Integrated Sensor Networks with Error Correction for Multiplexed Particle Tracking in Microfluidic Chips

Ningquan Wang,[a] Ruxiu Liu,[a] Norh Asmare,[a] Chia-Heng Chu,[a] and A. Fatih Sarioglu[*abc]

[a] School of Electrical and Computer Engineering, Georgia Institute of Technology, Atlanta, GA 30332, United States
[b] Parker H. Petit Institute for Bioengineering and Bioscience, Georgia Institute of Technology, Atlanta, GA 30332, United States
[c] Institute for Electronics and Nanotechnology, Georgia Institute of Technology, Atlanta, GA 30332, United States

Abstract
Spatial manipulation of suspended cells based on their properties is an essential part of numerous microfluidic assays. To further read and analyze the manipulation result, a microscopy system is typically required, which, however, increases the cost and reduces the portability of the entire system. As an alternative, a network of integrated Coulter sensors, distributed over a microfluidic chip, provide rapid and reliable detection of spatially-manipulated cells. Code-multiplexing of distributed Coulter sensors enables simplification of such integration by offloading the hardware complexity into advanced signal processing techniques that are needed to interpret the coded sensor outputs. In this work, we combine code-multiplexed Coulter sensor networks with an error-correction technique, a strategy typically used in telecommunication systems for controlling errors in data over unreliable communication channels. Specifically, we include redundancy in the physical sensor design to alleviate the ambiguity in the signal-decoding process, so that interfering sensor signals due to coincidently-detected cells can be resolved reliably. The presented sensor technology not only tracks the spatiotemporal state of cells under test but also measures their sizes and flow speeds. To demonstrate the sensor concept experimentally, we fabricated a microfluidic device with 10 distributed Coulter sensors designed to produce distinct signal waveforms and performed experiments with suspended human cancer cells to characterize the performance of the sensor platform.

Keyword
Coulter sensing; Microfluidics; Error-correction; Sensor network; Cell tracking; Cytometry

1. Introduction
Microfluidic devices offer exciting opportunities for analysis of biological samples at the cellular level by employing microscale phenomena that cannot often be recapitulated on the macroscale. From an operational perspective, a microfluidic platform is unique in that it can (1) bring together various force fields (e.g., mechanical, chemical, or electrical) within the same device and use them to implement complex discrimination criteria and (2) deterministically screen cell populations against those established criteria in a controlled microenvironment (Du et al., 2006; Huang et al., 2002; Nam et al., 2011; Sollier et al., 2009; Yamada et al., 2004; Zhu et

al., 2012). As such, microfluidic systems are not only sought after as experimental platforms for basic research (Sun et al., 2018; Zhang and Tadigadapa, 2004) but also employed as clinical microdevices for extracting detrimental cells out of complex matrices such as blood (Chu et al., 2019; Geislinger and Franke, 2013; Hoshino et al., 2011; Sarioglu et al., 2015).

While highly effective in manipulating cells, microfluidic devices lack a native sensing scheme and hence often act as upstream sample preparation elements prior to quantitative measurements, typically performed with a laboratory instrument such as a flow cytometer (Robert et al., 2011), an optical microscope (Hsu et al., 2008; Korny et al., 2011), or a mass spectrometer (Mellors et al., 2010). This disconnection between microfluidic manipulations and quantitative measurements is an important factor hampering the widespread adoption of these potentially revolutionary tools as quantitative assays outside of academic research laboratories, for example, in resource-limited or in point-of-care settings, where they can be truly transformative in healthcare delivery.

Cells can be probed by a variety of sensing modalities (Altintas et al., 2018; Liao et al., 2018; Prathap et al., 2019). Among these modalities, electrical detection of cells through impedance modulations across an aperture offers a robust, label-free, and high-throughput method that also forms the basis of widely used Coulter counters (Coulter, 1956; Coumans et al., 2014; Pal et al., 2014). In fact, Coulter counters are routinely used in applications ranging from hematology (Chhabra, 2018) to monitoring of water resources for pathogens (Zhe et al., 2007). Equally important is that similar electrical sensors can easily be implemented in microfluidic channels through the use of microelectrodes to create microfluidic devices with integrated electrical sensing (Errico et al., 2017). However, microfluidic devices employing electrical sensors are limited to counting, sizing, or measuring electrical properties (e.g., impedance spectroscopy (Iliescu et al., 2007)) of cells and cannot measure other cell properties that cannot be probed electrically.

We have introduced an electrical biosensor, Microfluidic CODES (Liu et al., 2016; Liu et al., 2017; Wang et al., 2017), that can transduce spatial manipulation of cells on a microfluidic device into an electrical signal in order to infer a variety of properties of a cell from its motion within the device. The Microfluidic CODES spreads a single Coulter counter across a whole microfluidic device by micropatterning its electrodes to create multiple measurement nodes, where the distinct electrode patterns produce location-specific signature electrical waveforms. By identifying these signature waveforms from individual measurement nodes through computational analysis of the output signal (Liu et al., 2018; Wang et al., 2019), one can electrically track the motion of cells within the device in lieu of imaging for cytometric analysis. Therefore, Microfluidic CODES not only provides a quantitative electronic output to plastic lab-on-a-chip devices while retaining their simplicity and frugality but also transforms Coulter sensing from a technique that is limited to sizing and counting of cells to a platform biosensor technology to analyze cells with respect to any parameter that can be used to differentially manipulate cells on a microfluidic device such as cell surface expression (Civelekoglu et al., 2019), mechanical properties (Asmare et al., 2019), and immunophenotype (Liu et al., 2019).

In this paper, we introduce a bioelectronic sensor network that combines the code-multiplexed read-out of the Microfluidic CODES and a microelectrode layout with built-in error correction for distributed Coulter sensing in microfluidic devices. We specifically introduce redundancy into the on-chip electrical sensor network and use it for error correction to minimize ambiguity in data processing. The built-in error correction allows us to relax design constraints on location-specific Coulter signatures, allowing the use of uncomplicated electrode patterns producing non-orthogonal sensor waveforms, while still ensuring reliable recovery of information through computation. Combined with machine learning algorithms, our approach allows us to account for not only device-to-device variations due to noise in the manufacturing of chips but also changes in device operation due to sample heterogeneity. We demonstrate the sensor operation in a prototype microfluidic device by processing a suspension of human tumor cells and validate the accuracy of our device through comparisons with high-speed microscopy.

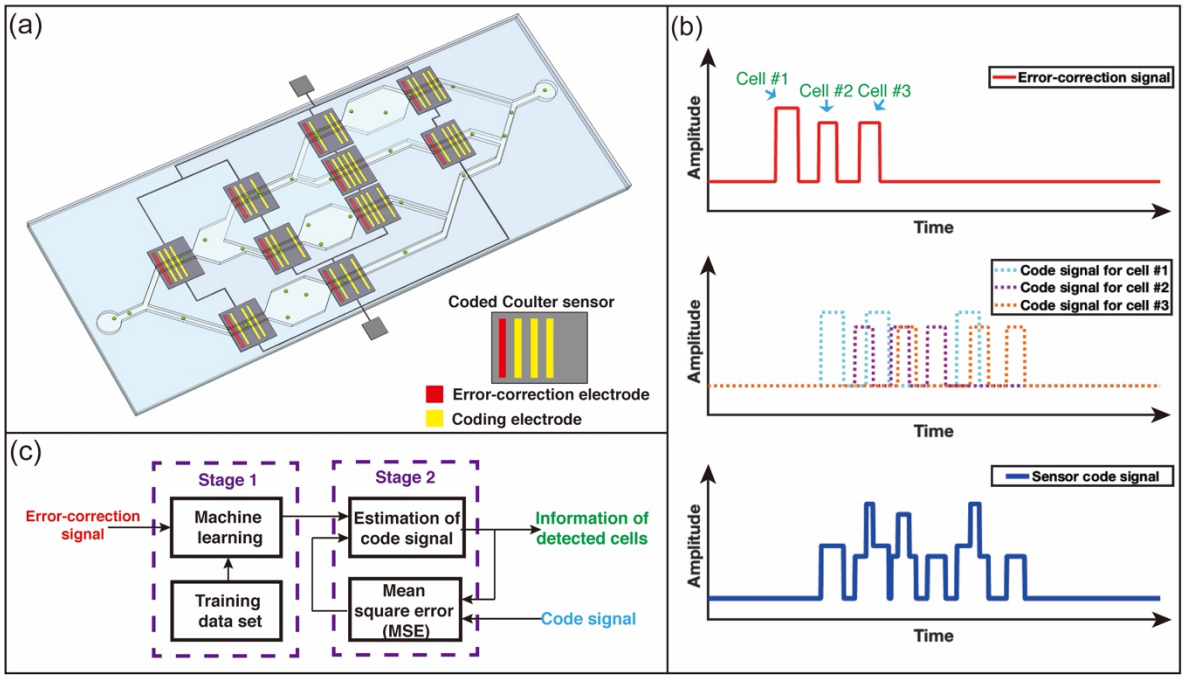

Fig. 1. *Sensor operation principle. (a) A network of Coulter sensors with distinct electrode patterns distributed at strategic locations on a microfluidic device. Within each individual sensor, an error-correction section was patterned beside a coding section to provide error-mitigating information. (b) Conceptual code-multiplexed sensor network signals. Each cell produces a single electrical pulse (i.e., the error correction signal) (top plot) and a corresponding code signal composed of a multitude of pulses (middle plot). Because the code signals consume more bandwidth, they interfere in the output signal (bottom plot). (c) A block diagram explaining the demultiplexing of interfering sensor code signals with the help of extra information provided by the error-correction signal (e.g., number of cells detected, relative timing, and size). First, error-correction signals were analyzed, and sizes and speeds of detected cells were estimated. Based on the information acquired from the error-correction signals, interfering code signals were demultiplexed, and sensor identities (locations) of detected cells were determined.*

2. Sensor Operation Principle

Our approach is based on a code-multiplexed network of Coulter sensors created by micromachined surface electrodes for distributed electrical sensing of cells flowing in channels across a microfluidic chip. In the sensor network, each sensor is encoded with a distinct digital code (signature), and based on which, surface electrodes are micropatterned to create distinct spatial arrangements of interdigitated electrode fingers at different locations on the microfluidic device (**Fig. 1a**). Therefore, when activated, different sensors generate distinct sensor waveforms, indicating cell presence in specific nodes on the microfluidic chip. Because all coded sensors share the same electrical output, we can demultiplex the information from the whole network by recognizing individual signature waveforms in the output signal. This analysis further allows us to extract the flow path of individual cells, which could further be used to infer the properties of cells, depending on which criteria was used to fractionate cells on the microfluidic device.

An important feature of the microfluidic sensor network technology introduced in this work is that it uses unipolar non-orthogonal digital codes to increase the multiplexing capacity. In a conventional code-division-multiple-access (CDMA) system, codes are specially designed to be orthogonal to each other (Dinan and Jabbari, 1998), ensuring minimal cross-correlations among different codes in the network, so that signals from different sources, encoded with these mutually-orthogonal codes, can be differentiated with the minimum crosstalk using matched filtering (Ulukus and Yates, 2004). For our technique, employing orthogonal codes (Gold sequences (Gold, 1967)) to encode Coulter sensors at different locations introduces challenges in scaling the sensor network. Specifically, larger sensor networks require encoding different sensors with longer orthogonal waveforms, leading to (1) more complex electrode layout and (2) more sensor interference due to coincident cells (Liu et al., 2018). Alternatively, more information can be packed into a waveform for a given signal duration (i.e., bandwidth) if non-orthogonal waveforms are used. However, the disadvantage of using non-orthogonal waveforms compared to orthogonal ones is the additional ambiguity in the decoding process. Specifically, the interference between sensors in the network from coincident cells causes output signals to be underdetermined for decoding due to the non-optimized crosstalk between non-orthogonal sensor waveforms.

To alleviate the ambiguity in the decoding of the interfering non-orthogonal waveforms from sensors, we integrate redundancy in our sensor design for error correction/mitigation, which is a technique commonly used in digital data compression/transmission (Hamming, 1950). Specifically, in our design, each sensor in the network shares an extra detector with a dedicated output in addition to the code-generating electrodes micromachined to produce distinct electrical waveforms linked to specific locations on the microfluidic chip. This extra detector is a conventional Coulter sensor and generates single-bit pulse signals (error-correction signals) that contain information on count, size, and flow speed of cells detected in a given time window (**Fig. 1b**). In the decoding process, this extra information is then used to prevent the misinterpretation of the code-multiplexed signal by eliminating erroneous outcomes that conflict with the error-correction signal (**Fig. 1c**). Because of its smaller footprint, the error-correction sensor is less prone to sensor interference from coincident cells and effectively sets

the multiplexing capacity of the code-multiplexed sensor network. Importantly, our approach decouples sensor network multiplexing capacity from the code complexity and allows the use of smaller sensors that lead to less coincidence while ensuring reliable recovery of information in the presence of interference.

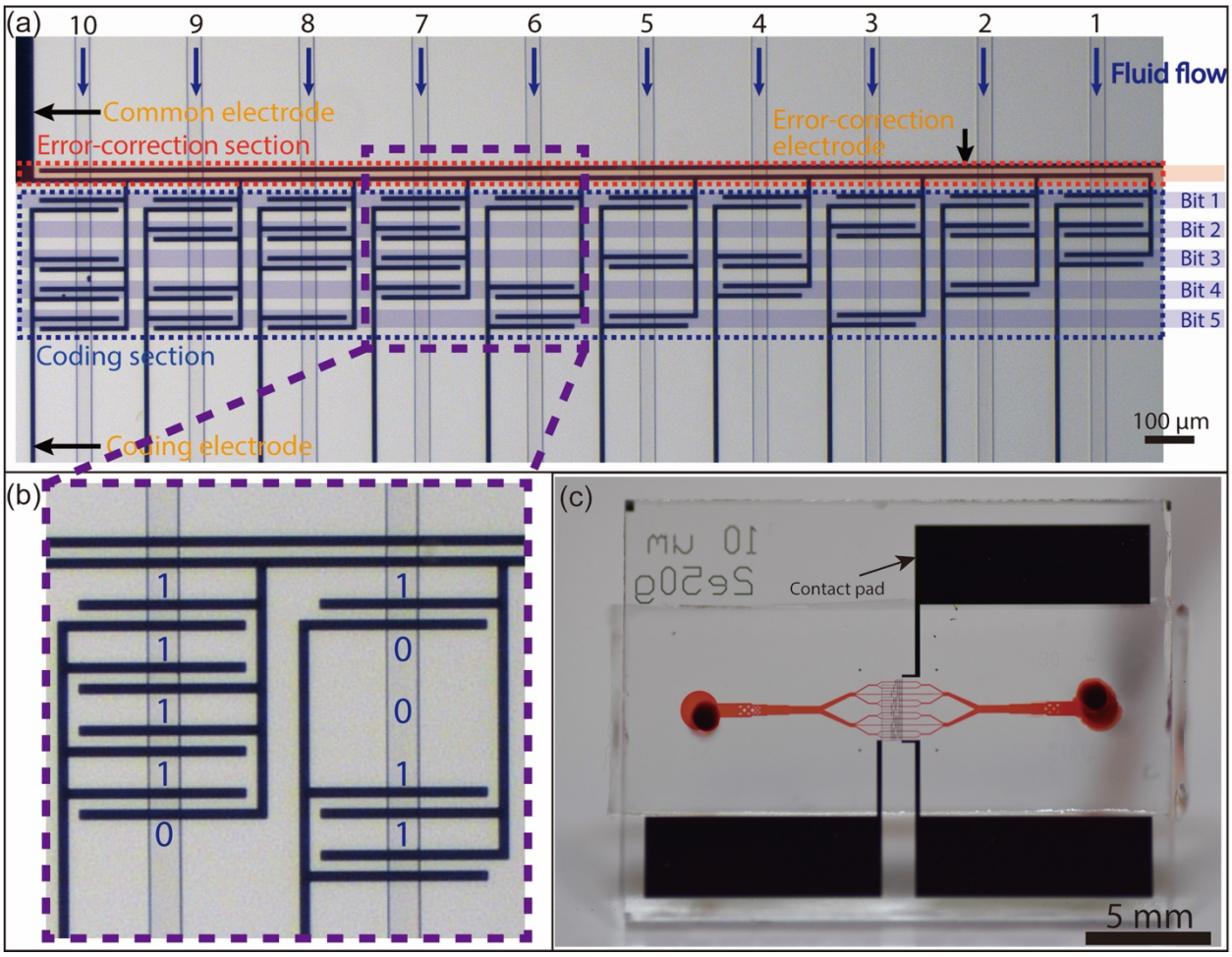

Fig. 2. *Design and layout of the microfluidic device integrated with coded Coulter sensor network. (a) A photomicrograph image of a 10-sensor microfluidic sensor network, in which a glass substrate patterned with Au electrodes was aligned and bonded with a PDMS layer with microfluidic channels. (b) A close-up view of sensor 6 and 7, which were micropatterned to generate codes of "10011" and "11110", respectively. (c) A photo of the complete microfluidic device used for our experiments.*

3. Microfluidic Device Design and Fabrication

For experimental testing of our sensors, we designed and fabricated an analytical microfluidic device integrated with a network of 10 code-multiplexed Coulter sensors (**Fig. 2a**). Without loss of generality, these 10 coded sensors were placed in close proximity so that all could fit in the field-of-view of a microscope. As such, the cell-sensor interaction could be visually observed as the ground truth for assessing the electrical system performance in this study. In practice, individual coded sensors could be positioned freely on the microfluidic by micromachining the metal film accordingly as demanded by the application at hand. In our sensor network, three coplanar electrodes, a common electrode, two sensing electrodes (an error-correction

electrode and a coding electrode) were micropatterned to form an error-correction section and a coding section for each sensor. In the designed layout, the common electrode was used to drive the entire sensor network with a voltage source, and the error-correction and the coding electrodes were used to measure the cell-induced impedance changes in the network by measuring changes in the electrical current flow.

While the minimum binary code length needed to distinguish 10 sensors was 4 bits, as $2^3 < 10 < 2^4$, we chose to encode each sensor in the network with 5-bit binary codes. This is because longer codes carried more information and could be identified with less ambiguity in the decoding process. On the other hand, sensor codes could not be extended excessively as decoding longer codes would lead to higher device complexity, more sensor interference, and additional computation time.

To implement these codes in the device, common and coding electrode traces were routed along opposite sides of a microfluidic channel and wherever a positive bit ("1") was needed, two 10 µm-wide electrode fingers, one from each trace, were extended into the microfluidic channel such that there was 10 µm gap between the two electrode fingers. Likewise, the absence of an electrode finger pair was interpreted as a negative bit ("0"), effectively creating sensors with assigned unipolar digital codes (**Fig. 2b**). Once interdigitated electrode patterns were aligned with microfluidic channels, the electrical current flow was confined to sections of the electrolyte-filled microfluidic channels that fell in between oppositely-charged electrodes. Therefore, it was only when cells occupied these electrically-active locations, that the electrical impedance was modulated, and the sensor output signal was produced.

In operation, cells flowing in microfluidic channels sequentially occupied electrically-active regions, producing a unipolar pulse sequence based on the underlying electrode pattern at that location. We specifically designed the electrode layout to generate isolated bit pulses in the code signals. First, we set the distance between adjacent electrode pairs, i.e., bits, to be larger than but close to the average cell diameter. This is because an excessively large gap would lower sensitivity and produce a less pronounced bit pulse. Second, we designed the neighboring fingers of adjacent electrode pairs to have the same polarity, i.e., both to be common or sensing electrodes. This layout ensured no electric field was present in between signal-generating electrode pairs. In addition, we designed the microfluidic channel height to be close to the average cell diameter to maximize sensitivity and also minimize variations in the cell-to-electrode distance. Nevertheless, this constraint could be relaxed to accommodate cell populations with large variations in size either by designing a higher microfluidic channel as small cells occupying a fraction of the channel height could still be detected (Liu et al., 2018), or by vertically focusing cells to the floor of the microfluidic channel (Tasadduq et al., 2017), which would guarantee high sensitivity and also minimize undesired variations the in the cell-to-electrode distance.

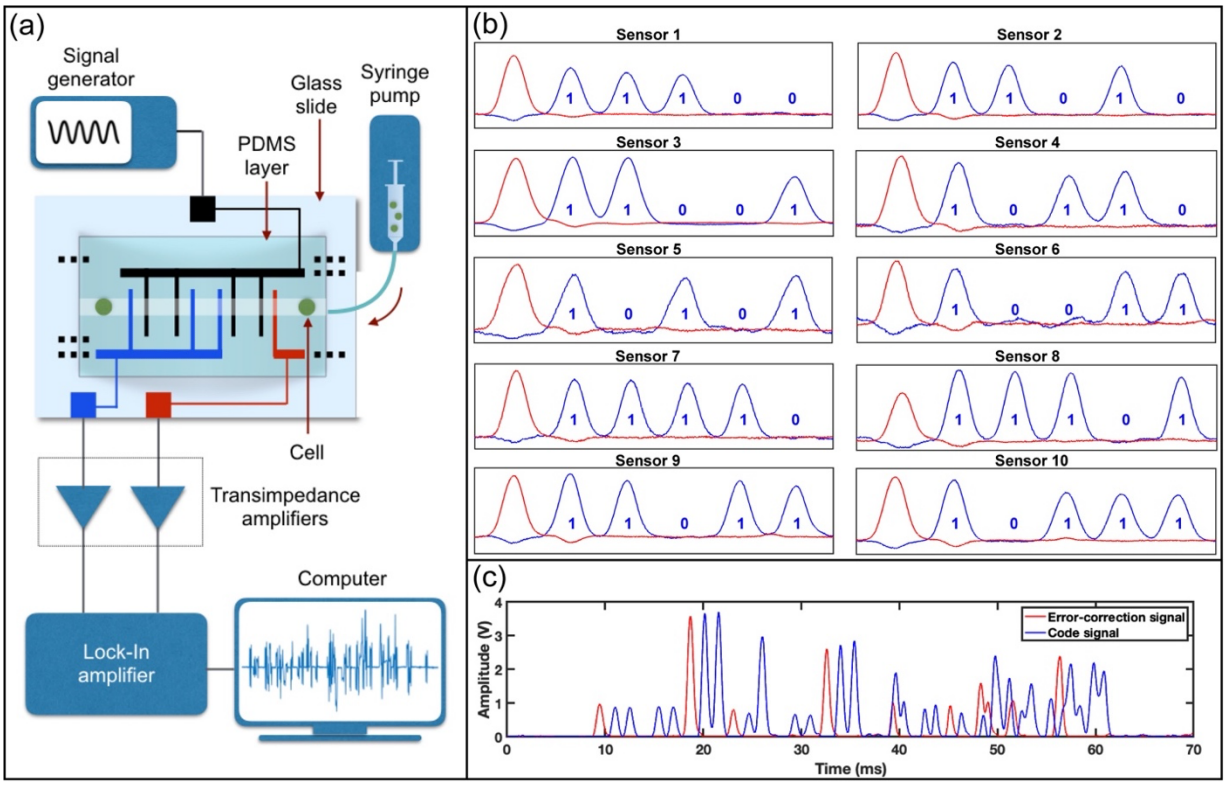

Fig. 3. *Sensor network data acquisition and testing sensor operation with cells flowing in the microfluidic device. (a) A schematic showing the experimental setup for driving the sensor network and acquiring sensor signals. (b) Recorded individual sensor signals generated by cells flowing in the microfluidic channels. Both error-correction signal (red) and the corresponding code signal (blue) are shown for every sensor in the network. The code (i.e., the sensor identity) could be determined from the number and timing of pulses in the recorded signal. (c) A recorded sensor network output signal where sensor code signals interfered due to multiple cells coincidentally detected by different sensors in the network.*

We fabricated our microfluidic device out of a polydimethylsiloxane (PDMS) layer patterned with microfluidic channels and a glass substrate layer patterned with surface electrodes. We patterned the PDMS layer using soft lithography. To create the mold, 15 µm-thick SU-8 photoresist (SU8-2015, MicroChem) was coated on a four-inch silicon wafer, and the photoresist was then patterned using conventional photolithography. The finished mold was then coated with PDMS prepolymer and cross-linker pre-mixed at a 10:1 ratio. The polymer film was degassed in vacuum and then cured in an oven at 65 °C for four hours. Cured PDMS was peeled off from the mold and cut into the final shape. We fabricated surface electrodes using a lift-off process. We coated a four-inch borosilicate glass wafer with 1.2 µm -thick negative photoresist (NR9-1500PY, Futurrex) and exposed the photoresist using photolithography to define the layout of the sensor network. Then we deposited 100 nm-thick Cr/Au film stack using e-beam evaporation. The underlying photoresist was etched in acetone. The finished wafer was diced into chips using a wafer saw. To create the final device, both the PDMS layer and the glass substrate were first surface-activated in an oxygen plasma and then aligned and bonded under a microscope (**Fig. 2c**). Copper wires were soldered to the electrode contact pads for the electrical read-out from the chip.

4. Sensor Testing and Data Acquisition

To test our sensors, we used human ovarian cancer cells (HeyA8) in suspension as a biological sample. Cells were grown in RPMI 1640 (Mediatech; Cellgro, Herndon, VA) with 10% fetal bovine serum (FBS; Seradigm, Radnor, PA). Cultures reaching >80% confluence were trypsinized and then resuspended in phosphate buffered saline (PBS). The cell suspension was then driven through the device by a syringe pump (Harvard 2000, Harvard apparatus) at a constant flow rate (500 μL/h).

To acquire the sensor response to cells flowing in the microfluidic channels, we excited the sensor network with an AC signal and measured the resulting current amplitude with a lock-in amplifier (HF2LI, Zurich Instruments) (**Fig. 3a**). The sensor network was excited from the common electrode with a 2-Vpp, 500-kHz sinusoid signal with a function generator. The excitation frequency was specifically chosen to (1) bypass the double-layer capacitance at the electrode-electrolyte interface, which was dominant at the low-frequency band and (2) prevent the Maxwell-Wagner dispersion at the high-frequency band (Valero et al., 2010). Electrical current signals from the error-correction and the coding electrodes were each converted into voltage signals using a transimpedance amplifier, and the signal amplitudes were measured by the two-channel lock-in amplifier. Signal amplitude information was then sampled at 50 kHz into the computer through a data acquisition board (PCIe-6361, National Instruments). It should also be noted that the sensor network could be driven at multiple frequencies simultaneously. This multi-frequency approach would then allow simultaneous measurements of cell size, speed, location along with dielectric properties (i.e., frequency response).

5. Results

5.1 Characterization of the Sensor Network

To characterize our sensor network, we analyzed error-correction and code signals from all sensors in the network (**Fig. 3b**). As expected, both signals were synchronized with the code signal pulses lagging the error-correction pulses with a delay that depended on the cell flow speed. Moreover, amplitudes of individual pulses increased with the size of the detected cell as the change in the impedance was proportional to the displaced volume of the electrolyte, according to the Coulter principle (DeBlois and Bean, 1970). Sensor code signals corresponding to detections of single cells were isolated from each other in the recorded output waveform and could directly be recognized as they closely matched the digital codes used to encode each sensor (**Fig. 3b**). For samples with high cell density, multiple cells coincidentally detected by the sensor network led to interferences of sensor waveforms and required further analysis to recover sensor identities, as will be explained later (**Fig. 3c**).

We also characterized the sensor code waveforms in terms of their uniformity. By comparing sensor code signals obtained from hundreds of cells for each sensor, we found that the amplitudes of pulses produced by the same cell varied from one bit to another (**Fig. 4a**). To investigate the signal variation across the sensor network, we fabricated microfluidic devices with a serpentine microfluidic channel (**Fig. S1a**), where a cell sequentially interacted with all the sensors in the network and allowed direct comparisons between waveforms from different

sensors in response to the same cell (**Fig. S1b**). By averaging normalized amplitudes for each bit in those recorded code signals, we were able to determine bit amplitude variation patterns across the sensor network (**Fig. 4a, 4b**). Furthermore, we observed these bit amplitude variation patterns to change in different devices with identical electrode patterns, a result we considered to be due to fabrication-related differences (**Fig. S1c**). On the other hand, the relative amplitudes of bits within a code signal were observed to not change significantly for different cells detected by the same sensor. For all sensors in the network, we measured the standard deviations for the relative amplitude of individual bits in normalized signals between different events (**Fig. 4c**) and concluded that the mean normalized amplitudes of bits for the sensor network could be used to construct a template library from recorded data to accommodate device- and sample-specific variations.

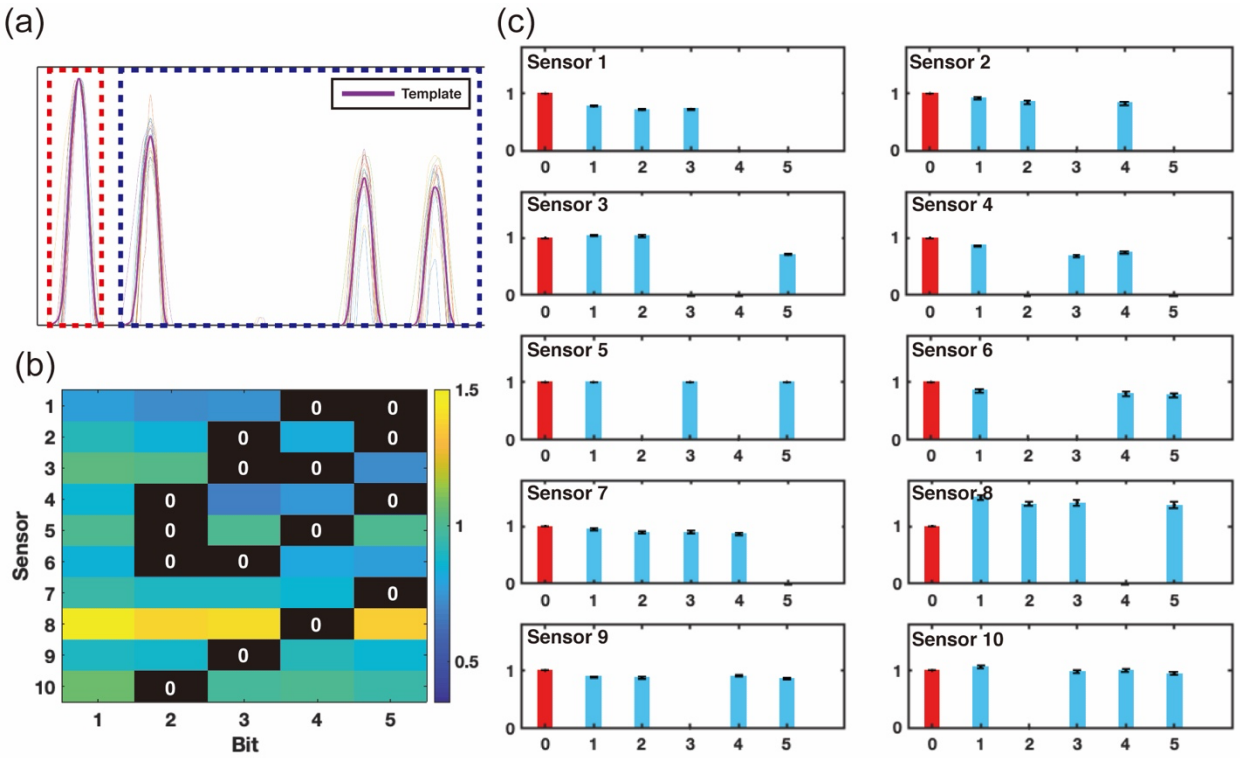

Fig. 4. *Analysis of code-multiplexed sensor signals. (a) An eye-diagram showing the signals corresponding to the sensor designed to produce the code "10011". Code waveforms for > 50 cells were normalized in amplitude and time and overlaid to demonstrate the code pattern integrity. We created a template signal for each sensor by averaging the signals from multiple cells. (b) A heat map showing the mean bit peak amplitudes in normalized code signals for all sensors in the network. All signals were acquired from cells sequentially interacting with every sensor in the network for direct comparison. (c) Measured mean and standard deviation of normalized bit amplitudes in sensor waveforms.*

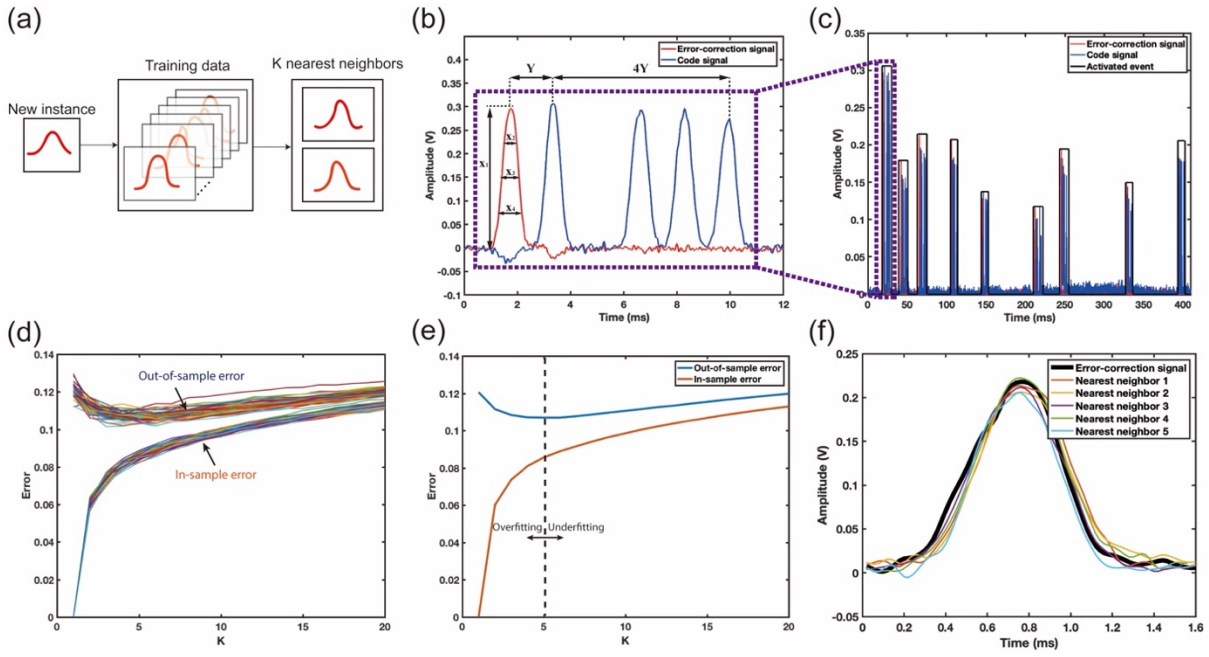

Fig. 5. *Analysis of the error-correction signal for estimating cell flow speed. (a) A schematic showing the employed machine learning technique, where the cell flow speed was calculated from K most similar error-correction pulse profiles found in the training data. (b) Representation of the error-correction signal with four extracted features: the peak amplitude, and the pulse widths at ¾, ½, and ¼ of the peak amplitude (x_1, x_2, x_3, and x_4). The cell travel time from the error-correction section to the coding section of the sensor (Y), was chosen as the property to be predicted and used to calculate the flow speed of the cell. (c) Automatic identification and aggregation of sensor signals from the raw sensor output to construct the training dataset. (d) Model performance in cell flow speed predictions as a function of the number of nearest neighbors (K) utilized in calculations (n=50). In-sample and out-of-sample error rates indicate the performance on the training data itself and a testing dataset, respectively. (e) Mean in-sample and out-of-sample error rates. K=5 yielded the lowest out-of-sample error and was chosen as the optimal value. (f) A representative error-correction pulse overlaid with its five nearest neighbors identified by our model.*

5.2 Analysis of the Error-correction Data

We analyzed the error-correction pulses to estimate the arrival time, size, and flow speed of cells. Among these parameters, the arrival time information was readily accessible as an error-correction pulse was produced each time a cell was detected by our sensor network. The cell size was estimated from the peak amplitude of the error-correction pulse according to the Coulter principle. We calibrated the electrical data through linear regression of the cubic root of the error-correction pulse amplitude versus the cell radius measured by high-speed microscopy (**Fig. S2**). Estimation of the cell flow speed was achieved by analyzing the full profile of the error-correcting pulse as described below since the pulse duration could not directly be attributed to cell flow speed and was also affected by the cell size and the electrode geometry.

We developed a machine learning-based model to predict the cell flow speed from the profile of the error-correction pulse. Our model employed the *K*-nearest neighbors (*K*-NN) algorithm (Bezdek et al., 1986), which searched the training data set for the *K* most similar (i.e., minimum Euclidean distance) instances and averaged their values to make a prediction (**Fig. 5a**). To represent the error-correction pulse profile, we extracted four features (X_1, X_2, X_3, and X_4 representing the peak amplitude and the pulse width at ¾, ½, and ¼ of the peak amplitude, respectively) (**Fig. 5b**). We chose the cell travel time from the error-correction section to the coding section (Y) as the property to be estimated. Combining the predicted cell travel time with known sensor dimensions, we could calculate the cell flow speed (60 μm / Y) and estimate the duration of the code waveform (4*Y) (**Fig. 5b**).

To test the accuracy of the *K*-NN model, we trained our machine-learning algorithm, evaluated its error rate under varying parameters, and optimized computational design based on characterization results. To train our model, we constructed a dataset with >1000 sensor waveforms, which was aggregated by automatically screening the raw sensor network data and identifying timeframes with sensor activity (**Fig. 5c**). For each cell detected, we directly extracted four features from the error-correction pulse (X_1 to X_4) and recorded the corresponding travel time (Y). To evaluate the performance of our *K*-NN model, we used the two-fold cross-validation (Burman, 1989). Briefly, we first randomly split the dataset into two equal halves. Then we evaluated the model by training the model on one half and testing on the same half (i.e., in-sample testing) and also by training the model on one half while testing on the other half (i.e., out-of-sample testing). In this process, each signal in the testing subset was treated as a new instance, and the cell travel time (Y) was predicted by searching and averaging the *K* nearest neighbors in the training subset. An overall error rate was calculated from the average deviation of the prediction from the actual value. This process was performed for *K* values ranging from 1 to 20 and repeated for 50 times for statistical power (**Fig. 5d**). We found that lower *K* values made the model with high-variance and more noise-prone (i.e., overfitting), while increasing the *K* value excessively made the model biased and prevented it from catching subtle differences (i.e., underfitting). The optimal value of *K* was determined as five, which yielded the minimum average out-of-sample error rate (10.5%) (**Fig. 5e**). When tested, the optimized algorithm was able to find five error-correction pulses that matched well in profile to the sensor data and averaged cell speed values associated with these pulses to predict cell flow speed (**Fig. 5f**).

5.3 Analysis of Coded Sensor Data

We analyzed the coded sensor data to recover signals from individual sensors in the network based on the template libraries and information acquired from the analysis of the error-correction signal. In this decoding process, for each error-correction pulse, we first generated 10 signature waveforms accounting for all sensor codes in the network (**Fig. 6**). When generating these candidate signals, (1) the peak amplitudes were determined based on the cell size estimated from the error-correction pulse and also on the previously generated template library (Section 5.1), which provided the ratios between amplitudes of different pulses in the candidate waveform, (2) the candidate waveform duration and the delay between signals were set based on the estimated cell flow speed (Section 5.2). Computer-generated waveforms were

then compared with the actual signal, and the one yielding the minimum mean square error (MMSE) was identified as a match to determine the sensor identity. This analysis scheme was also successful in decoding interfering sensor signals due to coincident cells. To decode interfering code signals, error-correction pulses were first used to determine the number, sizes, and flow speeds of coincident cells (**Fig. 6a**), and 10^N different signal combinations (**Fig. 6b**) were evaluated to find the matching combination with MMSE (**Fig. 6b**), where *N* was the number of cells coincidently detected in a given time interval.

Besides interfering code waveforms, we observed cases, where error-correction pulses from different sensors also interfered (**Fig. S3a**). In these cases, high cell density in the suspension led to multiple cells coincidentally interacting with error-correction electrodes despite their significantly smaller footprint than coding electrodes. To recover data in those instances, we first deconvolved interfering error-correction pulses. First, a peak-search algorithm was used to determine the number of contained individual pulses in the error-correction signal. Second, a curve-fitting algorithm was used to fit the interfering error-correction signal with a certain number of individual Gaussian-shaped pulses with different amplitudes and durations (**Fig. S3b**). Gaussian-shaped pulses were specifically chosen in this fitting process because the profile of a resistive pulse followed a Gaussian profile (Zhou et al., 2018). Estimated error-correction pulses were then analyzed individually according to the decoding process explained earlier to estimate cell size and speed (**Fig. S3c**), and based on these parameters, the corresponding code signal was estimated (**Fig. S3d**).

5.4 Testing of Sensor Network Accuracy

To evaluate the accuracy of our sensor network, we compared the results from the decoded electrical data stream to the simultaneously recorded microscope images, regarded as the ground truth, and calculated error rate in our measurements. In order to capture fast-flowing cells, images were acquired by employing an optical microscope equipped with a high-speed camera (Phantom v7.3, Vision Research) set to record cell flow across the whole sensor network at 1000 frames per second.

To automatically analyze the electrical data from the sensor network, we implemented our decoding algorithm in MATLAB. To perform the decoding of sensor waveforms on a continuous data stream, we combined the MMSE fitting (Section 5.3) with a moving-window approach. Briefly, we processed the output signal three error-correction pulses at a time. Once the decoding of a timeframe was completed, the window was shifted by one error-correction pulse, and the process was iterated until the whole data stream was decoded. The computational complexity of this process scaled as $O((N-M+1)*10^M)$, where 10 is the number of code-multiplexed sensors, *N* is the total number of cells detected in the time interval, and *M* is the number of cells analyzed at a time within the moving window, respectively.

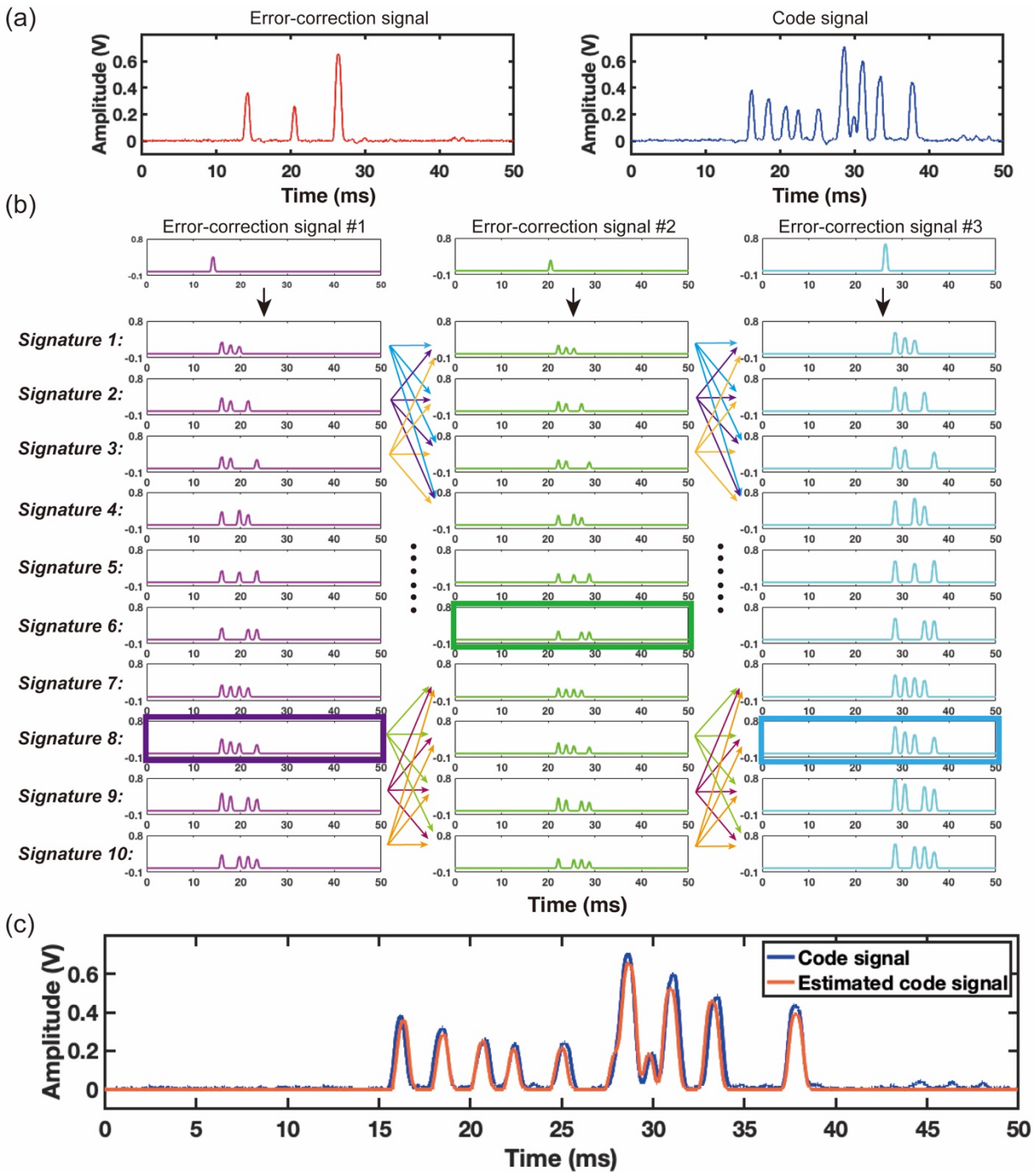

Fig. 6. *Decoding of interfering sensor signals due to coincidentally detected cells. (a) A recorded error-correction signal and the corresponding code signal. The error correction signal clearly indicated the detection of three cells. (b) For each error correction pulse, 10 candidate code signals were digitally generated based on the estimated cell flow speed and the preconstructed waveform templates. Given three cells were detected, 10^3 possible signal combinations were constructed. (c) The recorded code signal overlaid with the reconstructed waveform yielding the minimum mean square error. The solution showed the three cells were detected by sensors 8, 6, and 8.*

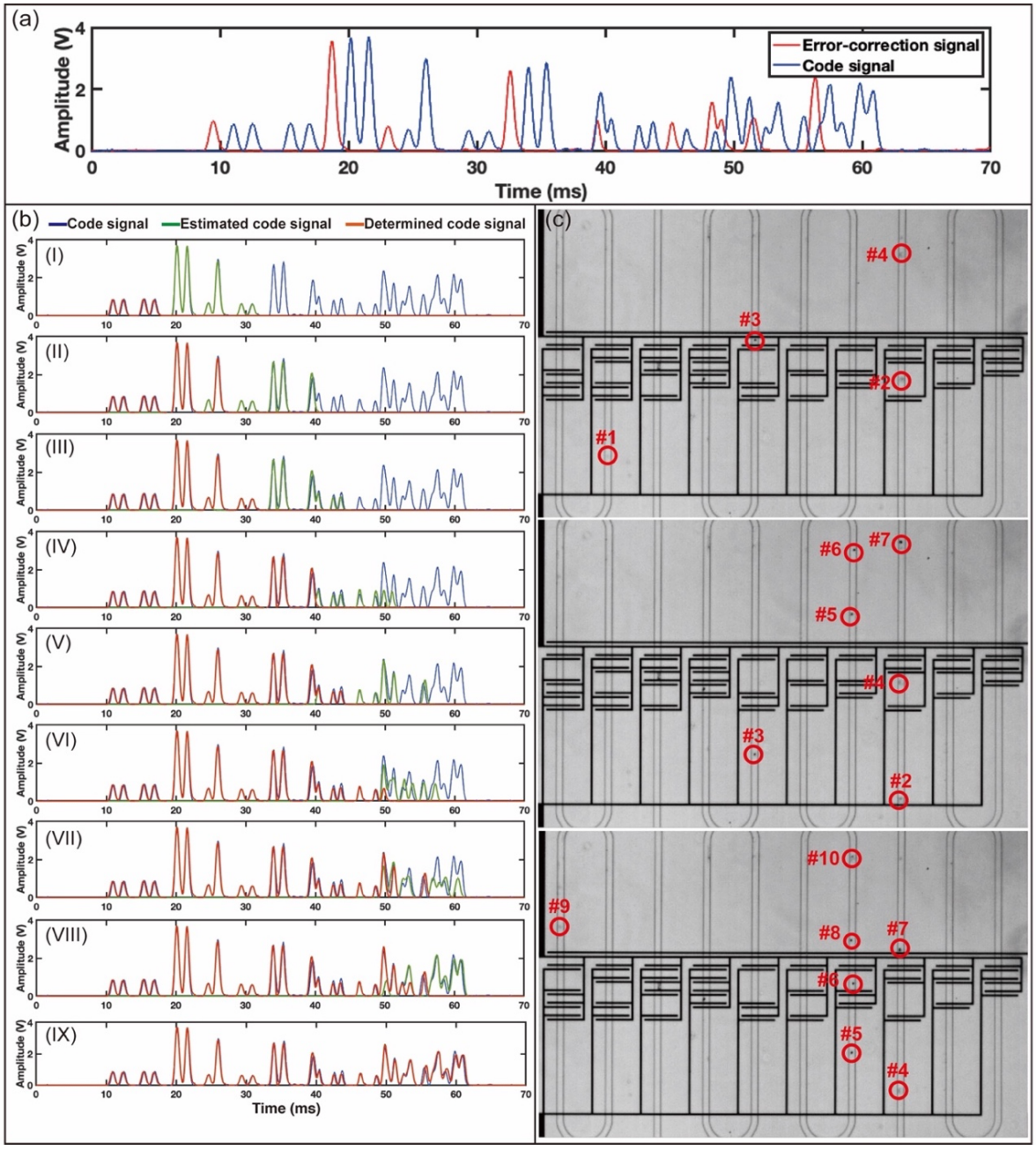

Fig. 7. *Testing of the sensor network cell tracking accuracy. (a) A section of a recorded output signal that contains data from 10 cells detected by the sensor network in a 70-ms time interval. (b) Plots showing the iterative decoding of the sensor waveform through a sliding window, which screened three error-correction pulses at a time. Each subplot shows the transient state of the fit at that iteration of the decoding process. At the end of the decoding process, the fitting code signals provided the identity of sensors detecting the cells and the timing of these events. (c) Frames sampled from the high-speed microscope footage of the cells simultaneously-recorded with electrical data. The data from the images matched the results from the sensor network.*

A direct comparison of processed sensor signal blocks with corresponding microscope images showed successful tracking of cells over the sensor network (**Fig. 7**). We investigated step-by-step decoding of a 70 ms-long time interval that contained data from 10 cells (**Fig. 7a**) as an example to illustrate coherence between electrical and visual data. Starting with the first window containing the first three error-correction pulses and sliding one pulse at a time, we were able to find a closely-matching estimation with the recorded experimental signal (**Fig. 7b**). Both sensor identities and the sequence of cell flow obtained from the decoded data agreed with the high-speed microscopy data (**Fig. 7c**).

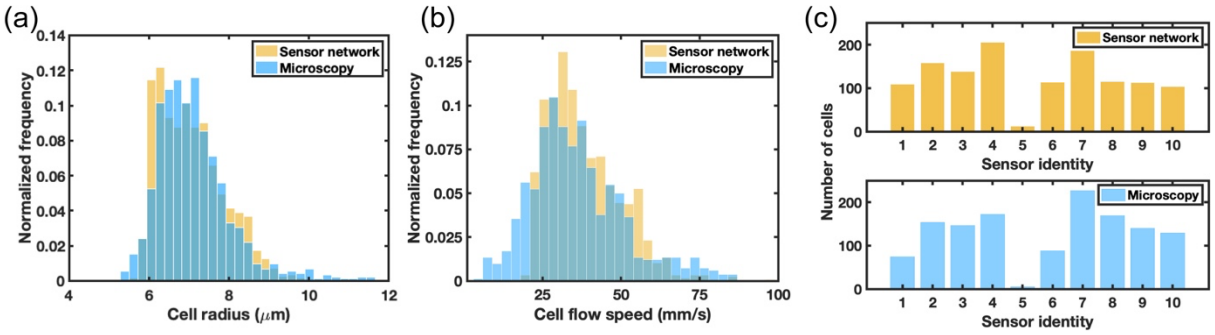

Fig. 8. *Benchmarking sensor network results against microscopy. (a) A histogram of the electrical and image-based measurements of cell size in populations sampled from the same culture (n=915). (b) A histogram showing the cell flow speed estimated by the sensor network and the measurement of cell speed by high-speed microscopy video footage (n=820). (c) Frequency of cells detected by each sensor in the network according to our electrical data (top plot) vs. the ground truth obtained by high-speed microscopy (bottom plot) (n=1304).*

To quantitively characterize the sensor network performance, we compared cell speed and sensor identity measurements from the electrical waveform and the associated high-speed video footage corresponding to >1200 cells. Due to the limited resolution of high-speed videos, we performed image-based cell size measurements with the ImageJ software on still, high-resolution microscope images of a surrogate cell population sampled from the same tissue culture (**Fig 8**). Optically-measured cell size distribution closely matched with that acquired from our sensor network (**Fig 8a**), with the Kullback–Leibler (KL) divergence between these two distributions calculated to be 0.044. Besides the errors introduced by the computational decoding process, the small divergence between the prediction and the ground truth came from the fact that the cells analyzed by the sensor platform and microscope were not the same population. Optically-measured cell flow speed distribution matched well with that acquired from the sensor platform, especially for flow speeds between 20 and 70 mm/s. (**Fig 8b**). Higher KL divergence (0.435) was mainly due to the mismatch in the lower end of the cell flow speed. Loss of accuracy with lower cell speed was due to the training dataset lacking cells with lower flow speeds, which could be improved by expanding the dataset to include a wider range of cell flow speeds. As for the accuracy of predicting sensor identity (i.e., spatial information), the success rate was measured as 90.07%, demonstrating cells could accurately be tracked with the on-chip sensor network (**Fig 8c**).

6. Conclusion

A multitude of integrated Counter counters, when each designed to produce a distinct sensor waveform, can simply be distributed across a microfluidic platform to provide spatiotemporal information from processed cells. Such information provides Coulter counters with the ability to analyze cell populations by monitoring cells' responses to various stimuli on the device besides their conventional use for sizing and counting cells. On the other hand, accessing information from all Coulter sensors in a scalable manner requires reliable demultiplexing strategies so that individual sensor data can be recovered with minimal loss. By introducing error-correction electrodes into coded Coulter sensors, we created a multiplexed sensor network, in which location-specific Coulter signatures could be realized with uncomplicated electrode patterns with relaxed design constraints. Testing the performance of the developed sensor network through direct comparisons with high-speed microscopy data showed that tumor cells could accurately be tracked on a microfluidic device in an integrated fashion. The ability to monitor cell motion with integrated on-chip sensors with minimal hardware overhead has the potential to enable quantitative cell/particle manipulation-based assays that can be deployed at the point-of-care.

Acknowledgement

This work was supported by the National Science Foundation, USA (Award no. ECCS 1752170), and the Arnold and Mabel Beckman Foundation, USA (Beckman Young Investigator Award to A. F. S.).

References

Altintas, Z., Akgun, M., Kokturk, G., Uludag, Y., 2018. Biosens. Bioelectron. 100, 541-548.
Asmare, N., Arifuzzman, AKM, Wang, N., Boya, M., Liu, R., Sarioglu, A.F., 2019. 20th International Conference on Solid-State Sensors, Actuators and Microsystems & Eurosensors XXXIII (TRANSDUCERS & EUROSENSORS XXXIII)
Bezdek, J.C., Chuah, S.K., Leep, D., 1986. Fuzzy Set. Syst. 18 (3), 237-256.
Burman, P., 1989. Biometrika 76 (3), 503-514.
Chhabra, G., 2018. J. Lab. Physicians 10 (1), 15-16.
Chu, C.H., Liu, R., Ozkaya-Ahmadov, T., Boya, M., Swain, B.E., Owens, J.M., Burentugs, E., Bilen, M.A., McDonald, J.F., Sarioglu, A.F., 2019. Lab Chip 19 (20), 3427-3437.
Civelekoglu, C., Wang, N., Boya, M., Ozkaya-Ahmadov, R. Liu, Sarioglu, A.F., 2019. Lab Chip 19 (14), 2444-2455.
Coulter, W.H., 1956. Proc. Natl. Electron. Conf., 12, 1034-1040.
Coumans, F.A., van der Pol, E., Böing, A.N., Hajji, N., Sturk, G., van Leeuwen, T.G., Nieuwland, R., 2014. J. Extracell Vesicles 3, 25922.
DeBlois, R.W., Bean, C.P., 1970. Rev. Sci. Instrum. 41, 909-916.
Dinan, E.H., Jabbari, B., 1998. IEEE Commun. Mag. 36 (9), 48-54.
Du, Z., Colls, N., Cheng, K.H., Vaughn, M.W., Gollahon, L., 2006. Biosens. Bioelectron. 21, 1991-1995.
Errico, V., De Ninno, A., Bertani, F. R., Businaro, L., Bisegna, P., Caselli, F., 2017. Sens. Actuators B 247, 580-586.
Geislinger, T.M., Franke, T., 2013. Biomicrofluidics 7, 044120.

Gold, R., 1967. IEEE Trans. Inf. Theory 13 (4), 619-621.
Hamming, R.W., 1950. Bell Syst. Tech. J. 29 (2), 147-160.
Hoshino, K., Huang, Y.Y., Lane, N., Huebschman, M., Uhr, J.W., Frenkel, E.P., Zhang, X., 2011. Lab Chip 11 (20), 3449-3457.
Hsu, C.H., Di Carlo, D., Chen, C., Irimia, D., Toner, M., 2008. Lab Chip 8, 2128-2134.
Huang, Y., Joo, S., Duhon, M., Heller, M., Wallace, B., Xu, X., 2002. Anal. Chem. 74 (14), 3362-3371.
Iliescu, C., Poenar, D.P., Carp, M., Loe, F.C., 2007. Sens. Actuators B 123 (1), 168-176.
Korny, T., Dominguez-Villar, M., Baecher-Allan, C., Hafler, D.A., Yarmush, M.L., 2011. Biosens. Bioelectron. 26 (5), 2707-2710.
Liao, Z., Wang, J., Zhang, P., Zhang, Y., Miao, Y., Gao, S., Deng, Y., Geng, L., 2018. Biosens. Bioelectron. 121, 272-280.
Liu, R., Wang, N., Kamili, F., Sarioglu, A.F., 2016. Lab Chip 16 (8), 1350-1357.
Liu, R. Waheed, W., Wang, N., Civelekoglu, O., Boya, M., Chu, C.H., Sarioglu, A.F., 2017. Lab Chip, 17 (15), 2650-2666.
Liu, R., Wang, N., Asmare, N., Sarioglu, A.F., 2018. Biosens. Bioelectron. 120, 30-39.
Liu, R., Chu, C.H., Wang, N., Ozkaya-Ahmadov, T., Civelekoglu, O., Lee, D., Arifuzzman, AKM, Sarioglu, A.F., 2019. Small, 1904732.
Mellors, J.S., Jorabchi, K., Smith, L.M., Ramsey, J.M., 2010. Anal. Chem. 82 (3), 967-973.
Nam, J., Lim, H., Kim, D., Shin, S., 2011, Lab Chip 11 (19), 3361-3364.
Pal, A.K., Aalaei, I., Gadde, S., Gaines, P., Schmidt, D., Demokritou, P., Bello, D., 2014. ACS Nano 8 (9), 9003-9015.
Prathap, M.U.A., Castro-Pérez, E., Jiménez-Torres, J.A., Setaluri, V., Gunasekaran, S., 2019. Biosens. Bioelectron. 142, 111522.
Robert, D., Pamme, N., Conjeaud, H., Gazeau, F., Iles, A., Wilhelm, C., 2011. Lab Chip 11, 1902-1910.
Sarioglu, A.F., Aceto, N., Kojic, N., Donaldson, M.C., Zeinali, M., Hamza, B., Engstrom, A., Zhu, H., Sundaresan, T.K., Miyamoto, D.T., Luo, X., Bardia, A., Wittner, B.S., Ramaswamy, S., Shioda, T., Ting, D.T., Stott, S.L., Kapur, R., Maheswaran, S., Haber, D.A., Toner, M., 2015. Nat. Methods 12 (7), 685-691.
Sollier, E., Rostaing, H., Pouteau, P., Fouillet, Y., Achard, J.L., 2009. Sens. Actuators B 141 (2), 617-624.
Sun, X., Wang, H., Jian, Y., Lan, F., Zhang, L., Liu, H., Ge, S., Yu, J., 2018. Biosens. Bioelectron. 105, 218-225.
Tasadduq, B., Lam, W., Alexeev, A., Sarioglu, A.F., Sulchek, T., 2017. Sci. Rep. 7, 17375.
Ulukus, S., Yates, R.D., 2004. IEEE Trans. Inf. Theory 50 (5), 903-909.
Valero, A., Braschler, T., Renaud, P., 2010 Lab Chip 10 (17), 2216-2225.
Wang, N., Liu, R., Asmare, N., Chu, C.H., Sarioglu, A.F., 2019. Lab Chip, 19 (19), 3292-3304.
Wang, N., Liu, R., Sarioglu, A.F., 2017. J. Vis. Exp., 121, e55311.
Yamada, M., Nakashima, M., Seki, M., 2004. Anal. Chem. 76 (18), 5464-5471.
Zhang, Y., Tadigadapa, S., 2004. Biosens. Bioelectron. 19 (12), 1733-1743.
Zhe, J., Jagtiani, A., Dutta, P., Hu, J., Carletta, J., 2007. J Micromech. Microeng. 17, 304.
Zhou, J., Kondylis, P., Haywood, D.G., Harms, Z.D., Lee, L.S., Zlotnick, A., Jacobson, S.C., 2018. Anal. Chem. 90 (12), 7267-7274.

Zhu, T., Cheng, R., Lee, S.A., Rajaraman, E., Eiteman, M.A., Querec, T.D., Unger, E.R., Mao, L., 2012. Microfluid. Nanofluidics 13 (4), 645-654.